

# The future intensification of hourly precipitation extremes

Andreas F. Prein\*, Roy M. Rasmussen, Kyoko Ikeda, Changhai Liu, Martyn P. Clark and Greg J. Holland

**Extreme precipitation intensities have increased in all regions of the Contiguous United States (CONUS)<sup>1</sup> and are expected to further increase with warming at scaling rates of about 7% per degree Celsius (ref. 2), suggesting a significant increase of flash flood hazards due to climate change. However, the scaling rates between extreme precipitation and temperature are strongly dependent on the region, temperature<sup>3</sup>, and moisture availability<sup>4</sup>, which inhibits simple extrapolation of the scaling rate from past climate data into the future<sup>5</sup>. Here we study observed and simulated changes in local precipitation extremes over the CONUS by analysing a very high resolution (4 km horizontal grid spacing) current and high-end climate scenario that realistically simulates hourly precipitation extremes. We show that extreme precipitation is increasing with temperature in moist, energy-limited, environments and decreases abruptly in dry, moisture-limited, environments. This novel framework explains the large variability in the observed and modelled scaling rates and helps with understanding the significant frequency and intensity increases in future hourly extreme precipitation events and their interaction with larger scales.**

Short-term precipitation extremes cause flash floods, landslides, and debris flows in the entire CONUS<sup>6</sup>. Precipitation intensities are expected to increase by  $\sim 7\%$  per degree warming ( $^{\circ}\text{C}^{-1}$ ) according to the Clausius–Clapeyron (C–C) relationship<sup>2</sup>. However, temperature scaling rates that are substantially larger than  $7\% \text{ } ^{\circ}\text{C}^{-1}$  have been found in mid-latitude observational records for sub-daily precipitation extremes at daily mean temperatures between approximately  $12^{\circ}\text{C}$  and  $22^{\circ}\text{C}$  (refs 7,8), while intensities are generally decreasing for higher temperatures because of moisture limitations<sup>4,9,10</sup>. The location of the breaking point (temperature above which intensities start to decline) is of particular interest since the highest precipitation intensities occur in these environments. So far it is not well understood whether the breaking point will shift due to global warming<sup>8</sup>. In addition, large variations of the temperature scaling rates were observed<sup>3</sup>, and a general framework to describe the mechanisms that control the relationship between temperature and sub-daily precipitation extremes is lacking at present<sup>8</sup>.

Convection-permitting climate models<sup>11</sup> are necessary to simulate observed hourly precipitation intensities<sup>4,11</sup> because their high resolution ( $\leq 4\text{ km}$ ) allows an explicit simulation of deep convection<sup>11</sup> whereas state-of-the-art low-resolution models have substantial biases in simulating sub-daily precipitation extremes<sup>12,13</sup>. Future climate assessments that used convection-permitting models show close to C–C scaling in the European Alps<sup>3</sup> and larger than C–C scaling in the UK<sup>14</sup>. Convection-permitting climate model simulations have been limited to small regions because of high

computational costs—raising questions about the transferability of their results to other regions.

Here we use a convection-permitting model with 4 km horizontal grid spacing to simulate the current and a possible future climate covering large parts of North America<sup>15</sup> (1,360 by 1,016 grid cells; Fig. 1 and Supplementary Fig. 1). These simulations allow the analysis of future changes in hourly extreme precipitation in various local climatic regions. The Weather Research and Forecasting Model (WRF)<sup>16</sup> is used to directly downscale the European Centre for Medium-Range Weather Forecast Interim Reanalysis (ERA-Interim)<sup>17</sup> data within the period October 2000 to September 2013 to the 4 km target grid. The first three months of the simulation are not included in the analysis so as to account for spin-up processes. The control simulation is able to reproduce the observed intensity and frequency of extreme hourly precipitation in most parts of the CONUS (see Supplementary Figs 2–4). The largest biases of  $-24$  to  $-40\%$  are found in the Central US during June, July and August (JJA). Care has to be taken when analysing climate change projections in this region, because biases of this magnitude might affect climate change assessments.

For the assessment of possible future changes, a pseudo global warming (PGW)<sup>18</sup> approach is applied. We perturb the lateral boundary conditions of ERA-Interim with a high-end scenario (RCP8.5) 95-year ensemble monthly mean climate change signal from 19 Coupled Model Intercomparison Project Phase 5 models<sup>15</sup> (CMIP5<sup>19</sup>; see Methods and Supplementary Table 1 for details). The resulting climate change response can be mainly related to thermodynamic processes and changes in the lapse rate, but also includes minor large-scale dynamic changes (for example, resulting from changes in the baroclinicity). The main dynamic characteristics of the weather patterns entering the domain boundaries and the moisture convergence patterns stay largely the same as in the current climate integration. The PGW method in combination with weak spectral nudging avoids the introduction of internal climate variability that could otherwise substantially influence climate change analyses of decadal-long simulations, but still allows the model to adjust for potential inconsistencies from domain internal climate change forcing. This approach is designed to isolate the thermal effects, and thus does not fully account for the effects of potential changes in weather patterns and synoptic-scale eddies that cause up to 20% of drying in Mexico and the US Southwest<sup>20</sup>, but the majority of the projected changes in precipitation are related to thermodynamic processes<sup>20,21</sup>.

The December, January and February (DJF) mean climate change signal shows decreasing precipitation south of  $30^{\circ}\text{N}$  and increasing precipitation to the north (Fig. 1a). The patterns agree with the climate change projections from the CMIP5

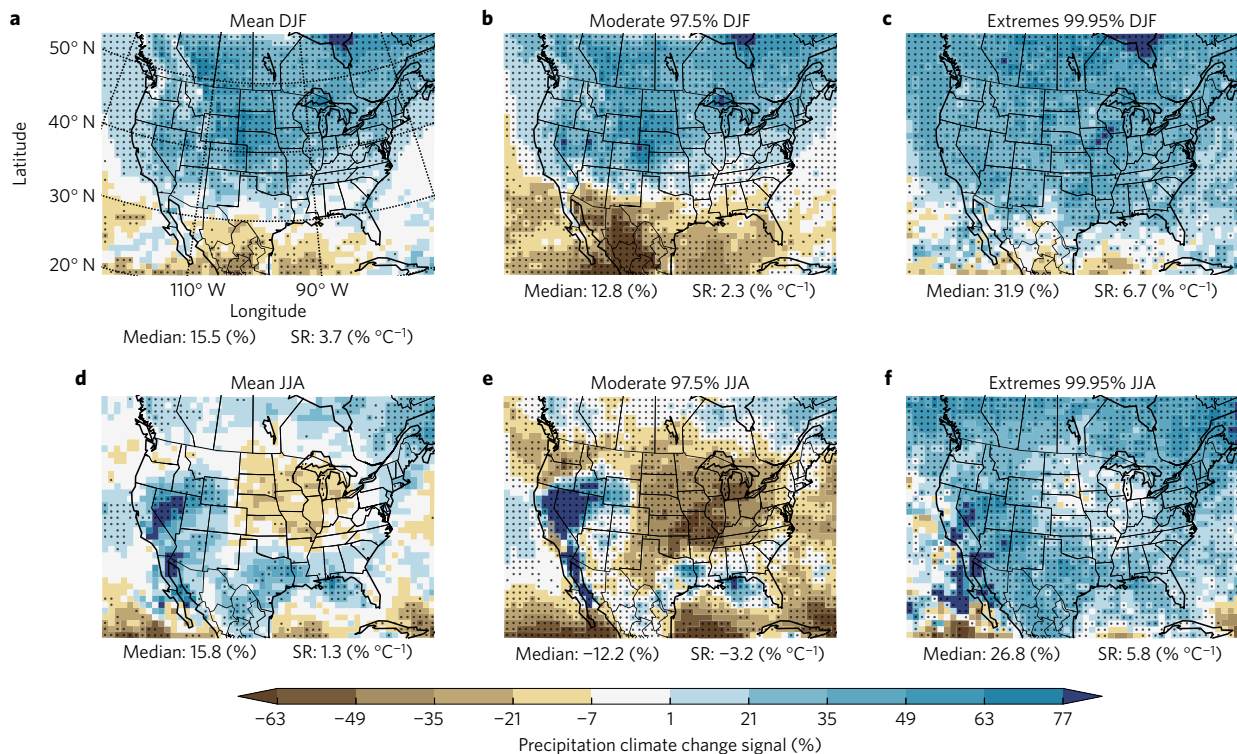


**Figure 1 | Hourly extreme precipitation is increasing in the majority of the domain, while mean and moderate intense precipitation are substantially decreasing in large areas.** Relative changes are shown for averages of  $25 \times 25$  grid boxes ( $\sim 100 \text{ km} \times \sim 100 \text{ km}$ ) to improve the signal-to-noise ratio for mean (a,d), moderate (97.5th percentile; b,e), and extreme precipitation (99.95th percentile; c,f). The spatial median change and average scaling rate (SR; precipitation change divided by seasonal mean temperature change) are shown below each map. Results are shown for December, January and February (DJF) (a–c) and June, July and August (JJA) (d–f). Dots highlight regions with significant changes. The investigated period is January 2001 to September 2013.

simulations<sup>21</sup>. Moderate intense precipitation events—defined as the 97.5th percentile of hourly precipitation—have a slight northward extension of drying trends (Fig. 1b), while extreme precipitation intensities (99.95th percentile) increase in nearly all regions (Fig. 1c). The 99.95th percentile of hourly precipitation corresponds to the maximum precipitation that occurs on average once every season. The domain median intensification of extreme precipitation is  $6.7\% \text{ °C}^{-1}$ . Increases in mean and moderate hourly precipitation are lower ( $3.7\% \text{ °C}^{-1}$  and  $2.3\% \text{ °C}^{-1}$ , respectively).

In JJA mean precipitation is increasing over most land areas except for the Central US and parts of the Pacific Northwest (Fig. 1d). The climate change signals are consistent with those from the CMIP5 projections<sup>21</sup> except for a more intense wetting in the US Southwest. The drying can be attributed to a significant decrease in moderate intense precipitation (Fig. 1e) that is counteracted by an increase in extreme precipitation intensities in the entire CONUS (Fig. 1f). The domain median extreme precipitation scaling rate is  $5.8\% \text{ °C}^{-1}$ , while the mean ( $1.3\% \text{ °C}^{-1}$ ) and moderate scaling rates ( $-3.2\% \text{ °C}^{-1}$ ) are substantially lower. Extremes in JJA intensify on average by 27%, with the largest increases in the US Southwest and Northeast and the smallest in the Midwest. The patterns of these changes qualitatively agree with observed trends of extreme daily<sup>1</sup> and hourly<sup>22</sup> precipitation and with climate change projections from coarse-resolution models<sup>23</sup>. However, the presented relative changes in hourly precipitation extremes substantially exceed global climate model (GCM) projections of increases in daily extremes in all regions except the Midwest<sup>23</sup>. It should be emphasized that the model has a significant dry bias in the Midwest during JJA, which might affect climate change projections in this region<sup>15</sup>.

The frequency of extremes increases by a factor of more than five in large parts of Canada and over the western US in DJF

(Fig. 2a). The frequency increase is much lower south of  $30^\circ \text{ N}$ . In JJA (Fig. 2b), frequencies increase by a factor of up to five in parts of the US Southwest, Mexico, and along the densely populated Gulf and Atlantic Coast. It is important to mention that actual frequency changes are sensitive to changes in weather patterns, which are assumed to stay constant in our simulations.

We examined the scaling rates between the 99th percentile of the daily maximum of hourly precipitation ( $P99_{d_{\max}}$ ) and daily mean temperature to better understand the processes that lead to increases in extreme precipitation intensities and frequencies (see Methods for details). The control simulation is able to capture the observed  $P99_{d_{\max}}$  intensities in the Southeastern subregion (Fig. 3a). Scaling rates (steepness of the curves) are close to the C–C rate for temperatures between  $0^\circ \text{ C}$  and  $24^\circ \text{ C}$ , and decrease afterwards<sup>4</sup>. The reason for the decreasing intensities at high temperatures is a transition into a moisture-limited environment. The total column relative humidity (TCRH; see Methods for the definition) at days with  $P99_{d_{\max}}$  events is clearly decreasing with temperature (Fig. 3b). TCRH can exceed 100% when inversions are present. Extreme precipitation scaling rates become negative if TCRH drops below a threshold. This threshold is  $\sim 54\%$  in low-elevation regions (below 500 m) and steadily decreases to  $\sim 35\%$  at higher elevations (above 1,000 m). With the help of this threshold, we can define two distinct environmental regimes. Wet regime environments (TCRH is larger than the threshold) are energy limited and positive scaling rates are supported, while dry regime environments are moisture limited and have negative scaling rates.

These two regimes also dominate the scaling rates in the future climate simulation, where the transition from the wet to the dry regime occurs at  $4^\circ \text{ C}$  warmer temperatures. This means that positive scaling rates are sustained up to  $\sim 30^\circ \text{ C}$ , resulting in

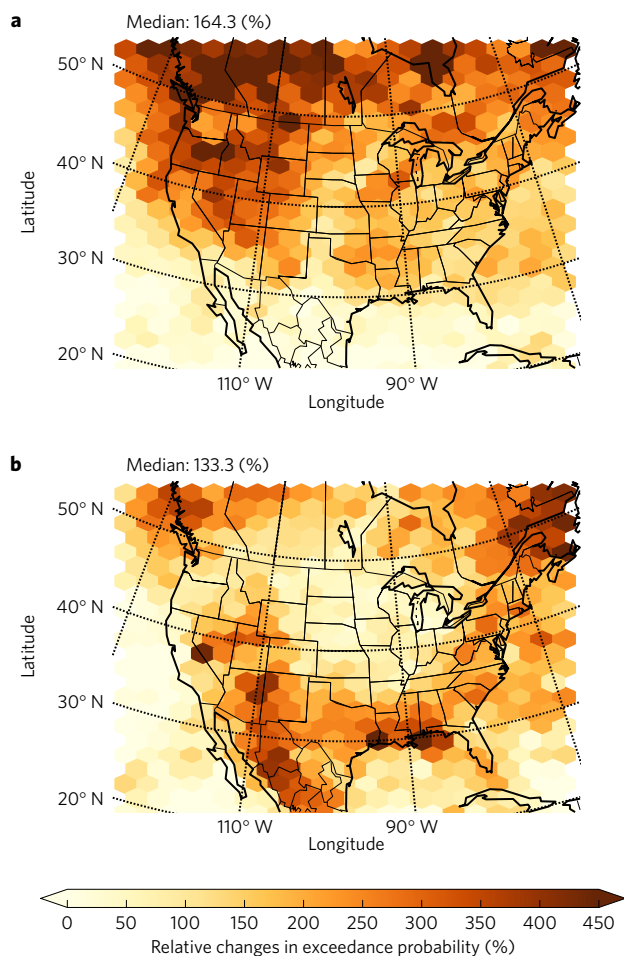


**Figure 2 | Relative changes in the exceedance probability of the control period 99.95th percentile of hourly precipitation intensities.** A value of zero indicates no changes in the probability of extreme precipitation while, for example, 300% means a fourfold higher chance of an extreme occurring. Results are shown for December, January and February (**a**) and June, July and August (**b**) for the period January 2001 to September 2013.

an intensification of the maximum  $P99_{d_{max}}$  from  $37 \text{ mm d}^{-1}$  to  $45 \text{ mm d}^{-1}$ . Climate change causes a shift of extremes-producing environments, which occur in the transition between the wet and dry regime, towards warmer and moister conditions, resulting in higher precipitation intensities, while the circulation patterns that cause extremes stay the same (Supplementary Figs 5–6). In general, the thermodynamic impact of climate change on precipitation scaling rates is a simple shift of the scaling curve along a  $7^\circ \text{C}^{-1}$  trajectory (Fig. 3g,h).

In the Pacific Southwest (Fig. 3c,d) TCRHs are close to the transition between the wet and the dry regime ( $\sim 54\%$ ) at cold temperatures (Fig. 3d) that results in close to zero scaling rates. Above  $12^\circ \text{C}$ , dry regime environments result in negative scaling rates in the observations. The observed scaling is well reproduced in the control simulation. In the future simulation,  $P99_{d_{max}}$  environments are warmer and moister, resulting in an intensification of precipitation intensities. This intensification occurs although past scaling rates are close to zero or negative, which clearly demonstrates that historical scaling rates cannot be used to assess information about future changes in extreme precipitation. See Supplementary Methods for a more detailed discussion.

The transition between the wet and dry regime in the Southern Rocky Mountains occurs at lower TCRHs of  $\sim 35\%$ , leading to an extension of positive scaling rates into drier environments (Fig. 3e,f).

This is typical for high-elevation regions ( $> 1,000 \text{ m}$ ) in the CONUS (see Supplementary Fig. 7). The control and future simulation also show an extension of positive scaling rates into drier environments, but peak at higher TCRH of  $\sim 49\%$ , resulting in an underestimation of precipitation intensities in the control simulation.

Considering all stations in the CONUS, observed scaling rates are positive for TCRH in the wet regime (above  $\sim 54\%$ ) while they abruptly decrease in the dry regime (Fig. 4a). The local maximum at  $\sim 45\%$  in the observations is related to the later transition into the dry regime at  $\text{TCRH} \sim 35\%$  at higher altitudes (above  $1,000 \text{ m}$ ; Fig. 4c). The scaling rates in the wet regime steadily increase with increasing TCRH, and are close to the C–C scaling for TCRH larger than  $90\%$ , which is dominated by the scaling rates from low-elevation stations (below  $500 \text{ m}$  Fig. 4b). The control simulation reproduces the dependence of the scaling rate on TCRH, but has an earlier transition into the dry regime (at  $57\%$  TCRH).

The future climate simulation shows a shift in the transition zone between the wet and the dry regime to higher TCRH values ( $\sim 63\%$ , Fig. 4a,b), as well as an increase of scaling rates for high TCRHs. The shift in the threshold might be related to the increase in atmospheric stability due to global warming<sup>24</sup>, which is supported by an increasing convection inhibition in the future climate simulation. The shift and the increased scaling rates originate from low-elevation regions (below  $500 \text{ m}$  Fig. 4b), since they do not occur at higher altitudes (above  $1,000 \text{ m}$  Fig. 4c).

In summary, we showed that hourly extreme precipitation events are projected to significantly increase in almost all North American land regions under the assumption that weather patterns in the future and current climate are similar. Increases in extreme frequencies of up to  $400\%$  are projected. These increases in hourly extremes substantially exceed the projected relative increases in daily extremes from GCMs<sup>23</sup> in all regions except for the US Midwest. The reason for the increase is a climate-change-induced shift of extremes-producing environments to moister and warmer conditions. We show that hourly precipitation extremes are also increasing in regions such as the Pacific Southwest, where no positive relationship between precipitation and temperature is observed. This implies that observed scaling rates cannot be used directly to assess climate change projections.

Our results do not show a super-adiabatic intensification of extremes, and are limited to  $\sim 7^\circ \text{C}^{-1}$ . This is in line with previous studies over the European Alps<sup>5</sup>, but is substantially smaller than rates found over the southern UK<sup>14</sup>, probably because of an inconsistent use of extreme indices<sup>25</sup>. It is important to mention that we do observe and model super-adiabatic scaling rates in some regions of the CONUS, but this does not relate to a super-adiabatic intensification of extremes in the future (see Fig. 3h).

The observed and modelled scaling rates are determined by a threshold in the climate system that depends on the moisture availability. Hourly precipitation intensifies with temperature in energy-restricted environments where moisture is not limited, while a rapid drop of scaling rates occur in moisture-restricted environments. This provides an as yet missing general framework<sup>8</sup> that unifies previous findings<sup>4,5,9,10</sup> and explains the large variations in observed and modelled scaling rates and future changes in scaling behaviours.

In future studies, this framework could be applied to investigate potential changes in scaling rates by analysing daily mean temperature and TCRH from coarser-scale models to assess uncertainties in future extreme events. Furthermore, we aim to investigate the effect of changes in the large-scale dynamics with GCM-driven convection-permitting climate simulations.

Our results indicate that there is a clear need to increase societal resilience to short-term precipitation extremes. The increase in the intensity and frequency of extreme precipitation would cause major challenges for existing infrastructure systems, as well as



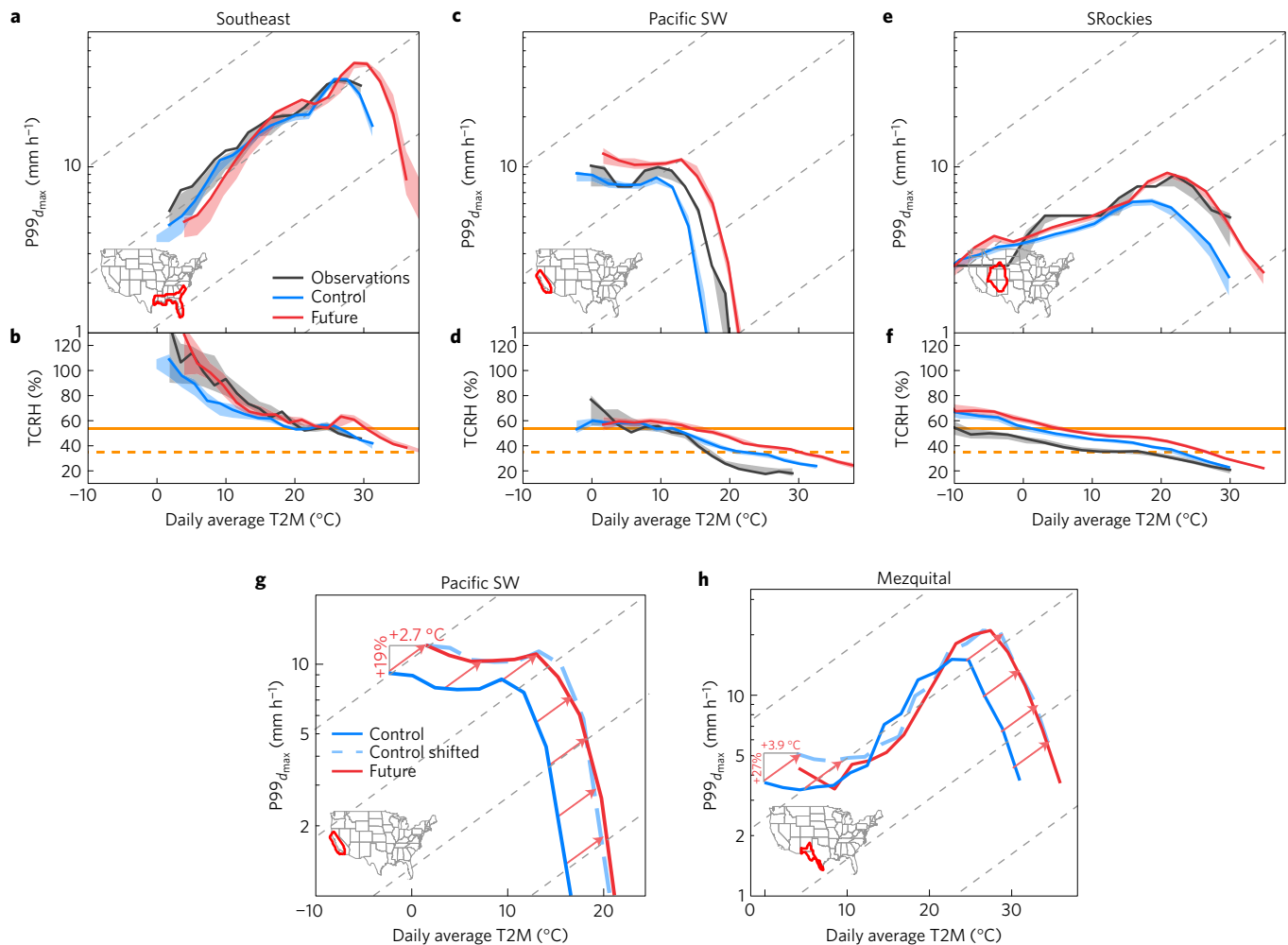


**Figure 3 | The scaling rates between daily mean temperature and extreme precipitation ( $P99_{d_{max}}$ ) are dependent on the available moisture in the atmosphere. **a,c,e**, Dependence of  $P99_{d_{max}}$  on surface temperatures. **b,d,f**, Dependence of total column relative humidity (TCRH) on the temperature at days with  $P99_{d_{max}}$  occurrence. In **a–f**, thick lines show the median values of the stations in the Southeast, Pacific Southwest, and Southern Rocky Mountains (left to right). Grey dashed lines in **a,c,e** show the C–C scaling and the orange solid and dashed lines in **b,d,f** depict the observed transition from the wet to the dry regime at low and high topographic elevations, respectively. Shaded areas denote the 98% confidence intervals computed by bootstrapping. **g,h**, The future scaling rates are very similar to the past scaling rates shifted by  $7\% \text{ } ^\circ\text{C}^{-1}$  (red arrows) as shown for the Pacific Southwest (**g**) and Mezquital subregions (**h**). Inset maps in figures show the locations of the subregions. T2M, temperature at 2 m.**

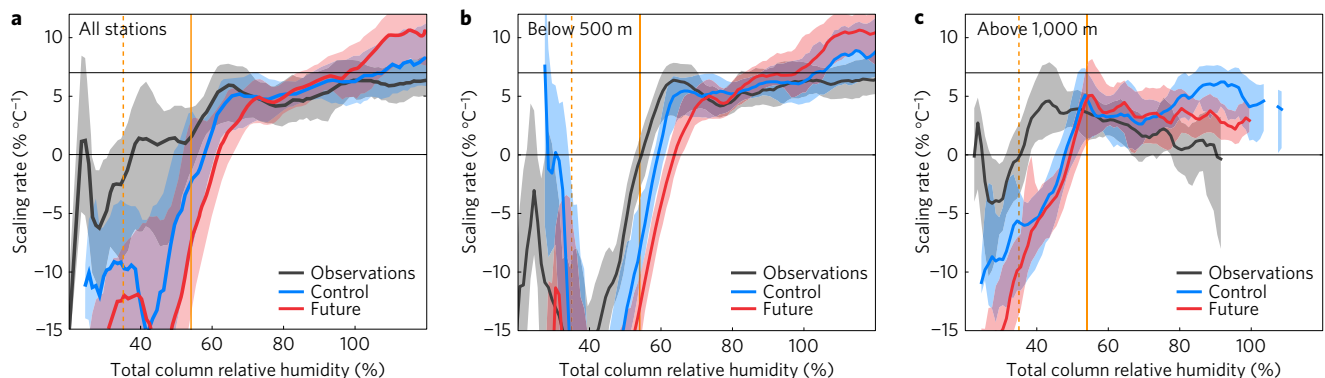


**Figure 4 | Positive scaling rates are supported if sufficient atmospheric moisture is available, whereas in dry environments negative scaling rates are present.** The thick lines show the median scaling rates in the CONUS and the shaded areas show the 25 to 75 percentile spread. To improve the signal-to-noise ratio, the average of all records in the surrounding of  $1^\circ$  around each station is calculated before the scaling rates are derived. The orange solid and dashed lines show the observed transition between the dry and the wet regime in low and high elevations. Results are shown for all stations (**a**) and for stations below 500 m (**b**) and above 1,000 m altitude (**c**) for the period January 2001 to September 2013.

demand fundamental reassessments of planning approaches to intense precipitation, local flooding, landslides, and debris flows.

## Methods

Methods and any associated references are available in the [online version of the paper](#).

Received 31 May 2016; accepted 28 October 2016;  
published online 5 December 2016

## References

- Kunkel, K. E. *et al.* Monitoring and understanding trends in extreme storms: state of knowledge. *Bull. Am. Meteorol. Soc.* **94**, 499–514 (2013).
- Trenberth, K. E., Dai, A., Rasmussen, R. M. & Parsons, D. B. The changing character of precipitation. *Bull. Am. Meteorol. Soc.* **84**, 1205–1217 (2003).
- Utsumi, N., Seto, S., Kanae, S., Maeda, E. E. & Oki, T. Does higher surface temperature intensify extreme precipitation? *Geophys. Res. Lett.* **38**, L16708 (2011).
- Chan, S. C., Kendon, E. J., Roberts, N. M., Fowler, H. J. & Blenkinsop, S. Downturn in scaling of UK extreme rainfall with temperature for future hottest days. *Nat. Geosci.* **9**, 24–28 (2016).
- Ban, N., Schmidli, J. & Schär, C. Heavy precipitation in a changing climate: does short-term summer precipitation increase faster? *Geophys. Res. Lett.* **42**, 1165–1172 (2015).
- Downton, M. W., Miller, J. Z. B. & Pielke, R. A. Reanalysis of US National Weather Service flood loss database. *Nat. Hazards Rev.* **6**, 13–22 (2005).
- Lenderink, G. & Van Meijgaard, E. Increase in hourly precipitation extremes beyond expectations from temperature changes. *Nat. Geosci.* **1**, 511–514 (2008).
- Westra, S. *et al.* Future changes to the intensity and frequency of short-duration extreme rainfall. *Rev. Geophys.* **52**, 522–555 (2014).
- Hardwick Jones, R., Westra, S. & Sharma, A. Observed relationships between extreme sub daily precipitation, surface temperature, and relative humidity. *Geophys. Res. Lett.* **37**, L22805 (2010).
- Neelin, J. D., Peters, O. & Hales, K. The transition to strong convection. *J. Atmos. Sci.* **66**, 2367–2384 (2009).
- Prein, A. F. *et al.* A review on regional convection-permitting climate modeling: demonstrations, prospects, and challenges. *Rev. Geophys.* **53**, 323–361 (2015).
- Kendon, E. J. *et al.* Do convection-permitting regional climate models improve projections of future precipitation change? *Bull. Am. Meteorol. Soc.* <http://dx.doi.org/10.1175/BAMS-D-15-0004.1> (2016).
- Jones, T. R. & Randall, D. A. Quantifying the limits of convective parameterizations. *J. Geophys. Res.* **116**, D08210 (2011).
- Kendon, E. J. *et al.* Heavier summer downpours with climate change revealed by weather forecast resolution model. *Nat. Clim. Change* **4**, 570–576 (2014).
- Liu, C. *et al.* Continental-scale convection-permitting modeling of the current and future climate of North America. *Clim. Dynam.* <http://dx.doi.org/10.1007/s00382-016-3327-9> (2016).
- Skamarock, W. C. *et al.* A Description of the Advanced Research WRF version 2 Technical note (NCAR, 2005).
- Dee, D. *et al.* The ERA-Interim reanalysis: configuration and performance of the data assimilation system. *Q. J. R. Meteorol. Soc.* **137**, 553–597 (2011).
- Rasmussen, R. *et al.* High-resolution coupled climate runoff simulations of seasonal snowfall over Colorado: a process study of current and warmer climate. *J. Clim.* **24**, 3015–3048 (2011).
- Taylor, K. E., Stouffer, R. J. & Meehl, G. A. An overview of CMIP5 and the experiment design. *Bull. Am. Meteorol. Soc.* **93**, 485–498 (2012).
- Emori, S. & Brown, S. Dynamic and thermodynamic changes in mean and extreme precipitation under changed climate. *Geophys. Res. Lett.* **32**, L17706 (2005).
- Maloney, E. D. *et al.* North American climate in CMIP5 experiments: part iii: assessment of twenty-first-century projections. *J. Clim.* **27**, 2230–2270 (2014).
- Muschinski, T. & Katz, J. Trends in hourly rainfall statistics in the United States under a warming climate. *Nat. Clim. Change* **3**, 577–580 (2013).
- Wuebbles, D. *et al.* CMIP5 climate model analyses: climate extremes in the United States. *Bull. Am. Meteorol. Soc.* **95**, 571–583 (2014).
- Frierson, D. M. Robust increases in midlatitude static stability in simulations of global warming. *Geophys. Res. Lett.* **33**, L24816 (2006).
- Schär, C. *et al.* Percentile indices for assessing changes in heavy precipitation events. *Climatic Change* **137**, 201–216 (2016).

## Acknowledgements

NCAR is funded by the National Science Foundation and this work was partially supported by the Research Partnership to Secure Energy for America (RPSEA) and NSF EASM Grant AGS-1048829. We thank the ECMWF and NASA for making available their data sets. Computer resources were provided by the Computational and Information Systems Laboratory (NCAR Community Computing; <http://n2t.net/ark:/85065/d7wd3xhc>).

## Author contributions

A.F.P. designed the study, and collected and analysed data. C.L. and K.I. performed and post-processed the climate simulations. All authors contributed to the writing process and gave conceptual advice.

## Additional information

Supplementary information is available in the [online version of the paper](#). Reprints and permissions information is available online at [www.nature.com/reprints](http://www.nature.com/reprints). Correspondence and requests for materials should be addressed to A.F.P.

## Competing financial interests

The authors declare no competing financial interests.

## Methods

**Observational data sets.** We use hourly precipitation data from 2518 stations included in the National Climate Data Center DSI-3240 data set<sup>26</sup> (Supplementary Fig. 1). We use only stations that have less than 20% missing values within the period 2001 to 2013. The daily mean near-surface temperature is derived from the PRISM 4 km gridded data set<sup>27</sup>. Daily average precipitable water (PW) data is derived from the ERA-Interim reanalysis. Using PW values from the Modern-Era Retrospective analysis<sup>28</sup> leads to very similar results. We apply inverse distance averages of the four closest grid cells around a station to derive station location estimates from the gridded observational data sets and the WRF model output, which is similar to previous studies<sup>4</sup>. Using hourly data to derive hourly extreme precipitation leads to a sampling-induced underestimation of hourly extreme intensities<sup>29</sup>. This underestimation does not significantly affect our results because of error cancellations in using hourly accumulations of observed and simulated precipitation (Supplementary Fig. 8).

**Climate simulations.** We performed sensitivity experiments with the WRF model to optimize its ability to simulate the current climate conditions over the CONUS<sup>15</sup>. Spectral nudging<sup>30</sup> of horizontal wind, temperature, and geopotential height was applied, starting at the planetary boundary layer (PBL), and increasing to the full strength at the fifth level above the PBL. A moderate nudging strength (coefficient) corresponds to an 'e-folding time' of about 6 h, which corresponds to the update frequency of the lateral boundary conditions. Wavenumber truncations of 3 and 2, corresponding to cutoff wavelengths of about 1,810 km and 2,030 km, were chosen in the zonal and meridional directions, respectively.

The PGW simulation is identical to the control simulation, but the ERA-Interim lateral boundary conditions are perturbed by average monthly mean high-end (RCP8.5) climate change signals between the period 2071 to 2100 and 1976 to 2005 from 19 CMIP5<sup>19</sup> GCMs (GCMs; Supplementary Table 1). This means that the year-to-year variability at the boundaries does not change in the future climate period. The climate change forcing at 700 hPa is between 3 and 5 °C in winter and 4 and 6 °C in summer. Changes in wind speed are below 1 m s<sup>-1</sup> and changes in relative humidity are between -4 and 1%<sup>15</sup>. The perturbations are added to temperature, vapour mixing ratio, geopotential height, and wind at each vertical model level, and to the sea surface temperature in the interior of the model domain. The perturbation of all state variables ensures the physical consistency of changes. Since the control period (2000 to 2013) is affected by climate change compared to the baseline climate period (1976 to 2005), the analysed climate change signal is slightly larger than the difference between 2071 and 2100 and 1976 to 2005. This PGW approach is feasible to assess future climate change because the full climate changes signal from a GCM-driven RCM simulation can be decomposed into three additive terms: a large-scale thermodynamic effect; lapse-rate effect; and large-scale circulation change<sup>31</sup>. In our study, we investigate the climate change effects from the first and second components, while the contribution of the third component is accounted for regarding its seasonally evolving large-scale changes, but not regarding its associated changes in storm-track activity.

To test if climate change signals in mean precipitation are significant compared to the inter-seasonal variability, the Wilcoxon signed-rank test is applied<sup>32</sup>. The Mann-Whitney rank test<sup>32</sup> is used to test for significant differences of precipitation intensities above the moderate (97.5th percentile) and extreme precipitation (99.95th percentile) threshold of the current and future climate simulation. Changes are tested at a significance level of 0.01.

**Temperature scaling.** The daily maximum of hourly precipitation is calculated at each station. These values are discretized into two-degree temperature bins (with an overlap of one degree) and the 99th percentile is calculated for all records

(P99<sub>dmax</sub>). To avoid extrapolation we calculate P99<sub>dmax</sub> values only for sample sizes larger than 50 members. Spatial representations of the scaling rates and improved signal-to-noise ratios are derived by arithmetically averaging the P99<sub>dmax</sub> values from all stations within climate subregions<sup>33</sup>. We use the full data record, including zero values for our analysis, to account for future changes in frequency and intensity in hourly precipitation<sup>5,25</sup>.

Bootstrapping is applied to estimate sampling uncertainties in the scaling analysis. For each station, 100 artificial time series are created by resampling the P99<sub>dmax</sub> values (with replacement).

The total column relative humidity is calculated as the daily mean PW divided by the maximum PW (PW<sub>max</sub>). The latter is estimated according to the following formula:

$$\text{PW}_{\text{max}} = \frac{k(a-b)}{\alpha R} \int_{l_0}^l \frac{e^x}{(x-a)(x-b)} dx$$

$$l_0 = \frac{\alpha T_0}{T_0 + 237.29}$$

$$l = \frac{a(T_0 - \alpha z)}{(T_0 - \alpha z) + 237.29}$$

where  $T_0$  is the daily average near-surface temperature in Celsius,  $\alpha$  is the constant lapse rate (we use 4 °C km<sup>-1</sup>),  $R$  is the gas constant in cm<sup>2</sup> s<sup>-2</sup> K<sup>-1</sup>,  $z$  is the height of the column of air in millimetres (we used 11,000,000 mm), and  $a$ ,  $b$  and  $k$  are constants with the values 17.2693882, 131.5430392 and 379.90516, respectively<sup>34</sup>.

## References

26. Data Documentation for Data Set 3240 (DSI-3240) Hourly Precipitation Data (National Climatic Data Center, 2013).
27. Daly, C. *et al.* Physiographically sensitive mapping of climatological temperature and precipitation across the conterminous United States. *Int. J. Climatol.* **28**, 2031–2064 (2008).
28. Rienecker, M. M. *et al.* MERRA: NASA's modern-era retrospective analysis for research and applications. *J. Clim.* **24**, 3624–3648 (2011).
29. Hershfield, D. M. *Rainfall Frequency Atlas of the United States: For Durations from 30 Minutes to 24 Hours and Return Periods from 1 to 100 Years* (Department of Commerce, Weather Bureau, 1963).
30. von Storch, H., Langenberg, H. & Feser, F. A spectral nudging technique for dynamical downscaling purposes. *Monthly Weather Rev.* **128**, 3664–3673 (2000).
31. Kröner, N. *et al.* Separating climate change signals into thermodynamic, lapse-rate and circulation effects: theory and application to the European summer climate. *Clim. Dynam.* <http://dx.doi.org/10.1007/s00382-016-3276-3> (2016).
32. Wilks, D. S. *Statistical Methods in the Atmospheric Sciences* Vol. 100 (Academic, 2011).
33. Bukovsky, M. *Masks for the Bukovsky Regionalization of North America* (NCAR, 2012).
34. Varmaghani, A. An analytical formula for potential water vapor in an atmosphere of constant lapse rate. *Terr. Atmos. Ocean Sci.* **23**, 17–24 (2012).